Computers in Biology and Medicine 179 (2024) 108832

Contents lists available at ScienceDirect

Computers in Biology and Medicine

journal homepage: www.elsevier.com/locate/compbiomed

An efficient procedure for the blood flow computer simulation of patient-specific aortic dissections

Rubén Zorrilla [a,c], Eduardo Soudah [b,c,d,*]

[a] Departament d'Enginyeria Civil i Ambiental, Universitat Politècnica de Catalunya (UPC), Barcelona, 08034, Spain
[b] Departament de Resistència de Materials i Estructures a l'Enginyeria, Universitat Politècnica de Catalunya (UPC), Barcelona, 08034, Spain
[c] International Center for Numerical Methods in Engineering (CIMNE), Barcelona, 08034, Spain
[d] Departamento de Ciencia de los Materiales e Ingeniería Metalúrgica, Expresión Gráfica en la Ingeniería, Ingeniería Cartográfica, Geodésica y Fotogrametría, Ingeniería Mecánica e Ingeniería de los Procesos de Fabricación, Universidad de Valladolid (UVA), Valladolid, 47011, Spain

ARTICLE INFO

Keywords:
Cardiovascular diseases
Aortic dissection
Computational fluid dynamics (CFD)
Level set methods
Unfitted mesh methods
CutFEM

ABSTRACT

In this work we present a novel methodology for the numerical simulation of patient-specific aortic dissections. Our proposal, which targets the seamless virtual prototyping of customized scenarios, combines an innovative two-step segmentation procedure with a CutFEM technique capable of dealing with thin-walled bodies such as the intimal flap. First, we generate the fluid mesh from the outer aortic wall disregarding the intimal flap, similarly to what would be done in a healthy aorta. Second, we create a surface mesh from the approximate midline of the intimal flap. This approach allows us to decouple the segmentation of the fluid volume from that of the intimal flap, thereby bypassing the need to create a volumetric mesh around a thin-walled body, an operation widely known to be complex and error-prone. Once the two meshes are obtained, the original configuration of the dissection into true and false lumen is recovered by embedding the surface mesh into the volumetric one and calculating a level set function that implicitly represents the intimal flap in terms of the volumetric mesh entities. We then leverage the capabilities of unfitted mesh methods, specifically relying on a CutFEM technique tailored for thin-walled bodies, to impose the wall boundary conditions over the embedded intimal flap. We tested the method by simulating the flow in four patient-specific aortic dissections, all involving intricate geometrical patterns. In all cases, the preprocess is greatly simplified with no impact on the computational times. Additionally, the obtained results are consistent with clinical evidence and previous research.

1. Introduction

With a global incidence between 2.5 and 7.2 cases per 100,000 [1], the aortic dissection (AD) is a severe cardiovascular disease (CVD) that stems from the separation of the inner (intima) and middle (media) layers of the aortic wall. This separation generates a false lumen that allows the blood to circulate through the aortic tissue, resulting in abnormal aortic haemodynamics and mechanical behaviour.

The AD survival rates are closely related to the progressive dilation, which is at the same time influenced by several factors such as the formation of new intimal tears, the intimal flap (IF) elasticity, the pressure jump between the true lumen (TL) and false lumen (FL), and the FL pressure value. Besides, the AD likely leads to other acute complications such as blood malperfusion, aneurysm formation and, in the worst scenario, rupture of the outer (adventitia) aortic tissue, which can cause mortality rates to reach up to the 50% depending on the patient's condition and the AD classification [2], which is based on the location of the dissection. Hence, in type A (or ascending) ADs the dissection appears either in the ascending aorta or in the aortic arch while in type B (or descending) ADs, which are the ones we mainly focus on, the dissection occurs in the descending aorta. Regarding the treatment, the rupture risk of type A ADs makes surgical intervention (aortic segment replacement or endovascular stent implantation) the preferred option. Concerning type B ADs, these normally develop into a chronic condition with high long-term morbidity and mortality rates owing to the recurrent dissections and eventual rupture. The intrinsic uncertainty and mortality rate of AD evince the need to provide clinicians with effective and efficient tools to support the therapy decision-making. Considering the inherent limitations of ex vivo models and experimental phantoms, numerical techniques, either in the form of computational fluid dynamics (CFD) or fluid-structure interaction (FSI) simulations, have a great potential to serve this purpose.

* Corresponding author at: International Center for Numerical Methods in Engineering (CIMNE), Barcelona, 08034, Spain.
E-mail addresses: rzorrilla@cimne.upc.edu (R. Zorrilla), esoudah@cimne.upc.edu (E. Soudah).

https://doi.org/10.1016/j.compbiomed.2024.108832
Received 12 March 2024; Received in revised form 6 June 2024; Accepted 29 June 2024
Available online 12 July 2024

It is widely known that one of the challenges appearing in the numerical simulation of CVDs is the efficient generation of the computational mesh from the medical images. In the particular case of the AD, the presence of an internal extremely thin layer of tissue introduces an extra complexity to such operation. As a first approach, one might consider to do a standard segmentation, that is to say, generating the TL and FL volumes such that their boundaries fit both the IF and the aortic walls. Though this is admittedly possible, it requires generating a volume mesh around a thin-walled body (*i.e.*, the IF), something that is well-known to be an extremely error-prone operation as the polygonal representations of each surface side tend to intersect each other when generating the boundary entities [3,4]. Consequently, the mesh generation becomes in an extremely effort- and time-consuming procedure, which compromises the applicability of standard computational techniques to AD scenarios.

In this work we aim at circumventing these complexities by introducing a novel methodology that targets the seamless simulation of patient-specific ADs. Our proposal starts by neglecting the thickness of the IF in order to completely decouple its segmentation from the TL and FL one. This results in what we called a two-step segmentation strategy, in which we first generate the volume (fluid) mesh from the segmentation of the outer aortic wall disregarding the presence of the IF. This effectively results in a procedure pretty similar to the one to be followed in a healthy aorta. Secondly, we create an independent surface (skin) mesh from the segmentation of the (approximate) midline of the IF. Once the two meshes have been generated, the original TL and FL configuration of the AD is recovered by "dropping" the surface mesh into the volume one and calculating a level set function [5] that implicitly represents the IF in terms of the volumetric fluid one. Although the level set-based description of the IF greatly simplifies the segmentation and mesh generation, it comes at the price of requiring an alternative wall boundary condition treatment as the fluid mesh no longer has nodes over the IF wall. For such purpose we leverage the well established unfitted (also known as non-conforming) mesh family of methods. In particular, we rely on a CutFEM approach that is capable to impose wall boundary conditions over immersed thin-walled bodies such as the IF.

Finally, it is important to make clear that in this work we do not consider the movement of the IF or, in other words, we simulate the AD as a rigid wall CFD problem. Nevertheless, we note that the methodology that we are proposing can be perfectly extended to account for the IF displacement, either in the form of a moving boundaries CFD or a fully-coupled FSI problem [6]. Indeed, unfitted mesh methods are known to perform extremely well in presence of large boundary displacements and rotations. Altogether, this makes us conceive this work as an intermediate but necessary step towards an efficient and robust methodology for the simulation of patient-specific ADs with possibly moving boundaries.

The article is organized as follows: Section 2 reviews the state-of-the-art; Section 3 details the methodology. This comprises the segmentation and mesh generation, the implicit representation of the IF via a discontinuous level set function and a brief explanation of the CutFEM method, which is our unfitted mesh method of choice; the governing equations and variational formulation are presented in Section 4; the patient-specific simulations setup and results are detailed in Section 5; the discussion of the results presented in Section 5 can be found in Section 6; and, finally, conclusions are summarized in Section 7.

2. State-of-the-art

2.1. Experimental and numerical simulation of type B ADs

Traditionally, the study of the AD has been conducted by means of experimental techniques. Focusing on type B ADs, it is possible to find successful applications of ex vivo models in [7,8] as well as experimental phantoms in [9–12]. Though these works proved that both ex vivo and phantom experiments can be used for the profound study of type B ADs, their inherent complexities and economic cost difficult their practical usage for the rapid-prototyping of patient-specific cases. Such limitations, combined with the constantly increasing computing power, led previous decade researchers towards considering numerical techniques as an alternative for the study and performance assessment of ADs. Hence, in [13,14] the authors used CFD simulations to validate previous ex vivo experiments of type B ADs. Similarly, [15–18] performed CFD simulations of patient-specific type B ADs. If one considers the most recent literature, it is easy to realise that current research targets accounting for the movement of the IF during the simulation or, in other words, solving the AD as an FSI problem. In this regard, we highlight [19–21] in which the authors exploit FSI methods for the simulation of idealised type B ADs. Similarly, in [22–26] the reader can find different studies and comparisons involving patient-specific ADs also based on FSI simulations.

At this point, it is important to make clear that even though all the previously mentioned works managed to appropriately perform CFD and FSI simulations of idealised and patient-specific ADs, all of them rely on standard mesh discretization techniques. Consequently, they all necessarily need to deal with the aforementioned segmentation and mesh generation complexities, something that turns into a much less efficient simulation pipeline that may eventually limit their applicability for the clinical decision-making. As previously mentioned, the primary objective of this work is to overcome such limitation by combining a two-step segmentation procedure with a level set-based unfitted mesh CFD method. As a difference to [27], in which we validated the aforementioned unfitted technique using results from four ex vivo experiments on idealised type B ADs [13], in this work we are applying our method to patient-specific cases. Compared to [27], dealing with real ADs naturally presents an additional challenge from the fluid simulation perspective. Furthermore, it requires the implementation of a seamless segmentation strategy (our proposed two-step approach) in order to efficiently deal with the much complex real geometries.

2.2. Unfitted mesh methods for the numerical simulation of CVDs

The main feature that distinguishes unfitted mesh methods from standard ones is the fact that (all or some of) the boundaries of the computational mesh do not match those of the analysed bodies, which are alternatively represented using a level set (distance) function [5]. Though the level set method is normally used to represent volumetric bodies (*i.e.*, bodies that feature internal volume), it can be also applied to track the position of thin-walled structures such as the IF. As it is discussed in [3], this requires switching from a standard continuous (nodal-based) signed distance function to a (potentially) discontinuous element-based one.

Once the unfitted boundaries are located via their corresponding level set representation, the boundary conditions can be imposed by using a wide variety variational approaches, leading to different families of techniques. Exploring all these methods in detail is beyond the scope of this work. Nevertheless, we highlight the eXtended Finite Element Method (X-FEM) [28–31], the Immersed Boundary Method (IBM) [32–35], the CutCell [36,37] and CutFEM [3,4,38], also known as Embedded Boundary Method (EBM), as well as the Shifted Boundary Method (SBM) [39–41]. Besides, [3,4,28,31,42] deserve special mention for presenting different approaches able to deal with IF-like thin-walled structures.

Unfitted mesh methods have been widely applied for the CFD and FSI simulation of cardiovascular systems. Among all of them, the IBM stands out as historically one of the most applied techniques, likely owing to its simplicity, which facilitated the FSI simulation of hearth valves since the early 70s [43–46]. Despite the IBM its continued use for the resolution of complex blood flow simulations [47], overcoming its intrinsic limitations motivated the apparition of highly advanced techniques such as the immersogeometric analysis [48,49]. More pertinent

to the approach we aim to follow in this work are the recent studies that use unfitted mesh discretization techniques to handle complicated CVDs geometries or to directly simulate over the 4D-PC-MRI images. Examples of these include [50], where the authors use a CutCell technique for the CFD analysis of the haemodynamics of an aortic stenosis model, and [51], which leverages an approach similar to the IBM to solve the haemodynamics of the mitral valve.

After reviewing the literature, it becomes apparent that the majority of applications of unfitted mesh methods to the numerical simulation of CVDs mainly focus on cardiac and valve dynamics. Only one very recent application to type B ADs can be found in the literature and, as a difference to our work, it does not consider an unfitted IF. Instead, the authors use immersed techniques to embed a stent geometry to assess its impact to the fluid flow after thoracic endovascular aortic repair (TEVAR) [52]. Hence, up to our knowledge there is no application of non-conforming mesh methods for the rapid-prototyping of patient-specific ADs. This is likely due to the limited number of unfitted approaches capable of handling thin-walled bodies compared to those designed for immersed bodies with internal volume. In this regard, we note that applying such techniques to the AD case is theoretically possible but would necessarily result in an exorbitant computational cost after the need of having a sufficiently fine mesh to account for the tiny thickness of the IF. As demonstrated later, our approach does not require any specific considerations for the volume mesh generation, meaning that the simulation times remain comparable to those of traditional techniques. Furthermore, our technique does not require the addition of extra degrees of freedom for the boundary condition imposition over the IF, unlike thin-walled approaches based on the X-FEM [28,31] or the use of Lagrange multipliers [48]. This represents a great performance advantage for the eventual extension to FSI problems, not only because the number of unknowns remains constant, but also because the sparse matrix graph does not need to be rebuilt during the simulation.

3. Methodology

Mesh-based numerical techniques can be roughly classified into body fitted (*i.e.*, body conforming) and unfitted (*i.e.*, non-conforming) techniques. Such classification is done according to how the mesh boundaries adapt to the analysed bodies geometries. Hence, in the traditional body fitted methods the mesh boundaries match those of the geometries of interest while this is not the case when using unfitted approaches. Instead, all or some of the boundaries are somehow dropped into the so called background mesh. Then, the immersed boundaries are implicitly represented in terms of the background mesh, typically by using a level set (*i.e.*, distance) function.

Though unfitted approaches come with some extra complexities, such as the need for an implicit boundary representation or a more complex imposition of boundary conditions, they have several advantages. The best-known one is the capability to naturally handle arbitrary large boundary displacements and rotations, thus skipping the need of remeshing due to mesh entanglement. Besides, there are other advantages related to the simulation preprocess which are of special interest in this work. The first one is the capability to deal with ill-conditioned input geometries. By ill-conditioned we mean CAD models featuring surfaces with undesired holes, overlaps or duplication that would require a huge amount of human work to be fixed to make the model compatible with standard meshing algorithms. The second one is related to the generation of volume meshes involving boundaries representing thin-walled (*i.e.*, membrane) bodies. This is known to be en error prone operation since the polygonal representation of the two sides of the membrane tend to intersect each other when generating the surrounding volume mesh.

In this work we aim to exploit these preprocessing capabilities for the efficient simulation of patient specific AD scenarios. Hence, we start by generating a volume mesh from the segmentation of the external aortic wall. We shall remark that such volume mesh is created disregarding the interior division in TL and FL. Then the division into TL and FL is introduced into the model by calculating the level set function representing the IF. The level set function is automatically computed by an algorithm from the intersections of a surface mesh representing the IF (obtained directly from the segmentation of the medical images). This makes it possible to alternatively locate the position of the IF within the volume mesh, thus allowing the imposition of the corresponding wall boundary conditions.

In the following subsections we detail each one of the previous steps. First we start by describing how we get the required meshes from the segmentation to then explain the basis of the implicit representation of immersed structures, with particular emphasis on the calculation of the discontinuous level set function. Next, we briefly discuss the usage of such level set in the context of the CutFEM to end the section by including a flow chart of the complete proposed methodology (Fig. 3).

3.1. Segmentation and mesh generation

In this work we analyse four patient-specific aortic dissection scenarios with distinct anatomical characteristics and challenges. We note that all the patients gave written informed consent for the scientific use of the radiological explorations and associated clinical data. Besides, all study procedures were conducted in accordance with the guidelines approved by the Ethics Committee and the Declaration of Helsinki. The scanning procedures were performed considering the standards of the manufacturer. The medical images required for the ADs segmentation are a CT scan of the patients' aorta. Such images were obtained by means of a 16-row multi-slice scanner and have a resolution of 0.625×0.625 mm, and an inter-slice distance of 0.6 mm covering the entire dissected aorta.

Our approach is based on a two-step procedure that consists on a first segmentation of the entire aorta, followed by a detailed segmentation of the IF (Fig. 1). For the first step, we use a semi-automatic technique that exploits active contour methods to accurately delineate the aorta outer boundary (*i.e.*, the aortic external wall). This approach avoids to initially distinguish the TL and FL, thus enabling a seamless segmentation of the entire aorta as all the complexities associated to the IF are completely bypassed at this stage. Subsequently, we construct a detailed mesh of aorta outer surface, from which the volume background mesh can be generated.

In a second step, we perform a detailed 3D segmentation of the IF. In this case the segmentation is not as simple owing to the intricate geometrical patterns (*e.g.*, tear shapes) appearing in the IF. Previous research explored methods such as graph-based techniques and spectral phase data to address similar challenges, namely variations in brightness and/or contrast as well as the artifacts appearing in CTA images [53,54]. More recent investigations also discuss innovative methodologies aimed at streamlining the segmentation procedure while improving its accuracy across different steps [55,56]. Considering that the focus of this article is not the IF segmentation process on itself but to leverage unfitted mesh methods to establish a robust methodology for the numerical simulation of ADs, we opt for a manual segmentation of the IF. To streamline the segmentation process, all scans were labelled under uniform conditions: a window width of 680 ± 15 HU and a window level of 310 ± 20 HU. This standardization minimizes irrelevant visual interference, ensuring consistency across visualizations. Nevertheless, we note that our approach has no limitation in this regard, meaning that the manual IF segmentation can be eventually upgraded in the future. Hence, the result of this second segmentation is a 3D (STL-type) surface mesh, which we remark is completely independent to the previous volume (background) one, that represents the IF's midplane.

Finally, we shall mention that the two-step segmentation process is crucial for the accurate representation of the AD as it makes possible to account for all the geometrical complexities of the IF. Furthermore, our proposal results in a much more robust and efficient generation

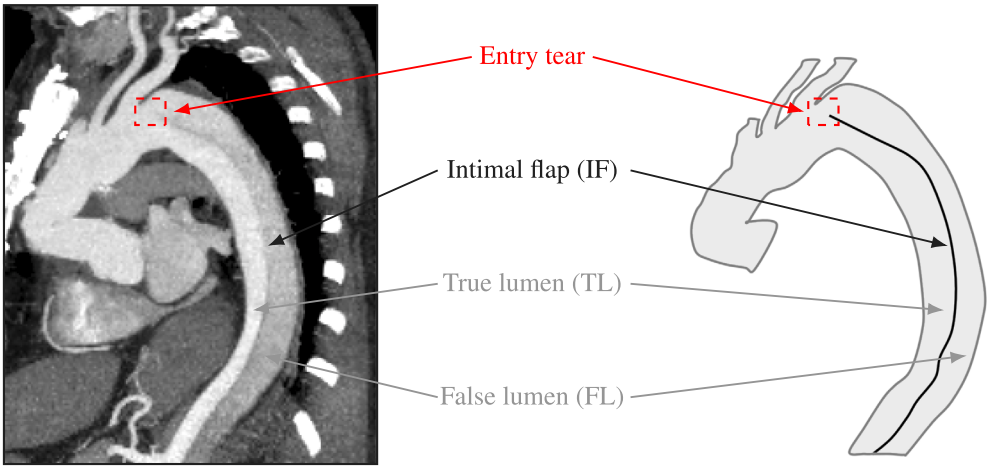

Fig. 1. Two-step segmentation procedure. Left: CT scan of a real AD. Right: sketch of the segmentation. The solid grey region represents the entire aorta (first segmentation step). The black line does so for the IF (second segmentation step).

of the computational meshes. About this, it is important to highlight that decoupling the volume and IF segmentation completely avoids the error-prone operations arising when trying to generate a volume mesh around a thin-walled body, something that becomes crucial when considering the geometrical artifacts inherent to the IF. In addition to this, neglecting the thickness of the IF, which is an assumption fair to be made, eases an eventual extension of the problem to the FSI case by enhancing the auxiliary surface mesh with shell (or membrane) formulation.

3.2. Discontinuous level set function

At this point we can distinguish two entities, a volumetric mesh representing the entire aorta and a surface mesh coming from the segmentation of the IF. We stress that the volume mesh is generated without taking into consideration the IF, something that, as already mentioned, greatly simplifies the segmentation. However, such improvement introduces the need of describing the IF segmentation using the volume mesh as a support for an implicit representation.

In a generic scenario, the implicit representation of the immersed bodies is achieved by the use of a standard level set (*i.e.*, distance) function that relies on the inside/outside concept [5]. Hence, those nodes of the volume mesh that are outside the embedded bodies have positive distance values. On the contrary, the volume mesh nodes lying in the interior of the immersed geometry have a negative distance value. In consequence, the zero isosurface of the distance field is indeed the representation of the analysed geometries' skin.

However, such nodal-based level set is not suitable for the IF case as the inside/outside concept makes no sense in presence of thin-walled bodies featuring negligible thickness. As it is described in [3], in this case one necessarily needs to switch to an element-wise distance. Hence, the idea is to calculate the intersections of each element of the background volume mesh with the surface elements representing the IF. Therefore, the level set is stored at the element level as a vector-valued magnitude which contains the distance from each intersected element's node to the IF. Consequently, the same node can have different distance value depending on the element considered. Because of this reason, this element-wise distance is also denoted as discontinuous level set.

Aiming at clarifying the discussion at hand, in Fig. 2 we present the discontinuous level set calculation workflow for a simplified case. Fig. 2(a) represents an ideal 2D AD scenario, from which we would eventually obtain the segmentation in Fig. 2(b). Hence, Fig. 2(b) involves two meshes, a volume (surface in 2D) one that comprises both the TL and FL regions and a surface (line in 2D) one that represents the IF. As depicted in Fig. 2(c), the identification of the TL and FL regions is achieved by embedding the IF mesh into the volume one and calculating the corresponding discontinuous level set function. This operation is schematically represented for a few representative elements, namely A, B and C.

The discontinuous distance calculation starts by searching for the possible intersections between each element of the volume mesh and the IF. This can be efficiently achieved by setting up an octree-based search structure from the IF mesh. If there are candidates to intersect, as it happens for instance in elements A and B, the next step is to compute the intersection points between the IF mesh and current element's edges (*i.e.*, line-line intersection in 2D and surface-line intersection in 3D), yielding the points denoted by rounds in Fig. 2(c). The intersection points allow to define the intersection plane (black dashed lines in Fig. 2(c)). Finally, the element distance vector entries are computed as the closest distance from each element's node to such intersection plane (*i.e.*, point-line distance in 2D and point-triangle distance in 3D). The sign of such distance values is set according to the orientation of the IF intersecting entities. On the contrary, if there are no intersections (element C) the distance vector entries are simply initialized to a constant positive (or negative) value. As depicted in Fig. 2(c), the sign of the elemental distances allows to define a positive (light green) and a negative (light red) distance region, thus implying that the IF can be locally tracked at each element as the zero value distance isosurface, which coincides with the intersection plane previously defined.

3.3. The CutFEM method

Though it implies an admittedly more intricate implementation, in this work we opt for the CutFEM technique owing to its optimal convergence and accuracy in the boundary representation. In particular, we follow the approach presented in [4] as it makes possible to solve the flow around thin-walled bodies without introducing extra degrees of freedom. We highlight that this avoids the need of modifying the sparse matrix graph, something that becomes crucial for the eventual extension of this work to the FSI case. The method presented in [4] is based on the substitution of the standard Finite Element (FE) space by an alternative one in those elements of background mesh that are intersected by the IF (*i.e.*, the elements featuring both positive and negative elemental distance values). Such alternative space, which we refer to as Ausas FE space after the name of the original author [57], is capable to represent the discontinuity in the velocity and pressure fields coming from the presence of the IF. The FE space substitution is complemented a relocation of the integration points (*i.e.*, subintegration) and a weak imposition of the boundary condition over the IF intersection (zero distance isosurface) by using the Nitche's method [58]. For further technical details the reader is referred to [59–64].

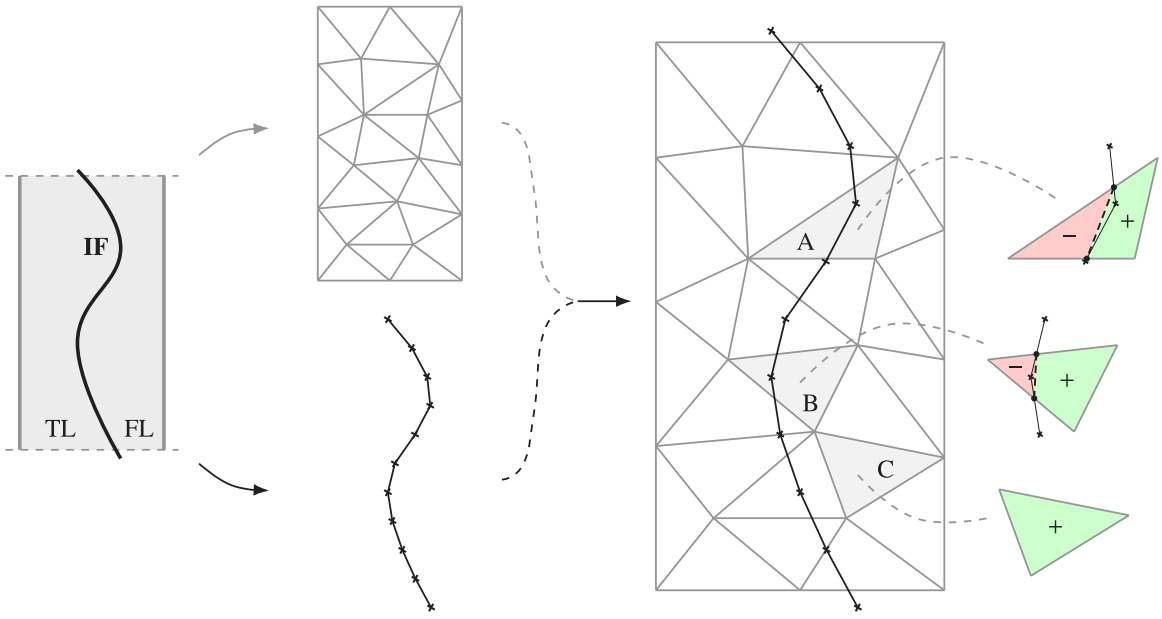

(a) Real scenario. (b) Segmentation. (c) IF embedding and distance calculation.

Fig. 2. Simplified 2D aortic dissection. Left: schematic representation of the simplified 2D problem. Centre: volume (top) and IF segmentation (bottom). Right: embedding of the IF segmentation and discontinuous level set calculation. The elements of interest A, B and C are highlighted in light grey. The round markers denote the IF and edge intersections. Black dashed lines represent the intersection plane stemming from the edge intersections. Light green and light red fill represent the positive and negative distance regions respectively.

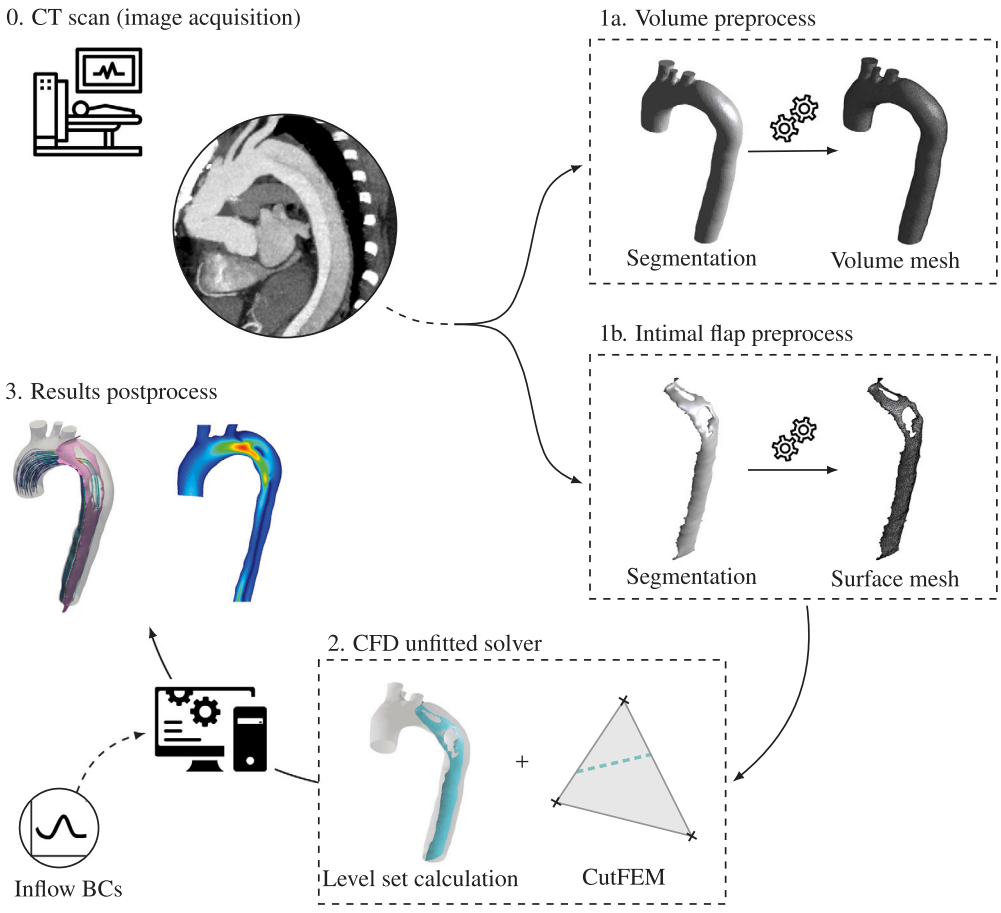

Fig. 3. Simulation flow chart. The two circle nodes attached to the dashed lines represent the required (patient-specific) inputs. The dashed rectangles highlight the main components of our proposal. These are the two-step segmentation procedure, from which the volume background and the IF surface meshes are obtained, and the unfitted CFD solver.

4. Formulation

In this section we briefly present the formulation. First we state the governing equations as well as their boundary conditions to subsequently present the corresponding variational form. Finally, we briefly discuss about the FE discretization and the stabilisation technique.

4.1. Governing equations

As it is customary in blood flow simulations, we neglect the compressibility of the fluid, meaning that the governing equations of the problem are the standard viscous incompressible Navier–Stokes equations. Hence, after denoting the fluid computational domain as Ω and the total simulation time as T, the problem to be solved can be expressed as

$$\rho \frac{\partial \mathbf{v}}{\partial t} + \rho \mathbf{v} \cdot \nabla \mathbf{v} - \nabla \cdot \boldsymbol{\sigma} - \rho \mathbf{g} = \mathbf{0} \quad \text{in } \Omega \times (0,T] \ , \tag{1a}$$

$$\nabla \cdot \mathbf{v} = 0 \quad \text{in } \Omega \times (0,T] \ . \tag{1b}$$

Here ρ is the fluid density, $\mathbf{v}$ and p are the velocity and pressure fields and $\mathbf{g}$ is the volume acceleration (*i.e.*, gravity). ∇ and $\nabla\cdot$ are the gradient and divergence operators, respectively. The Cauchy stress is denoted by $\boldsymbol{\sigma}$ and can be computed from the velocity and pressure fields as

$$\boldsymbol{\sigma} = \mathbb{C} \nabla^s \mathbf{v} - p \mathbf{I} \ , \tag{2}$$

being $\mathbb{C}$ the viscous constitutive tensor and $\nabla^s \mathbf{v}$ the strain rate tensor, which is defined as

$$\nabla^s \mathbf{v} = \frac{1}{2} \left(\nabla \mathbf{v} + \nabla \mathbf{v}^T \right) . \tag{3}$$

Eq. (1) needs to be completed with its corresponding boundary conditions. These are applied on the computational domain boundary $\partial\Omega = \Gamma$, which is defined as the union of the Dirichlet boundary Γ_D, the Neumann boundary Γ_N and the embedded boundary representing the IF, denoted as Γ_{IF}, such that $\Gamma_D \cup \Gamma_N \cup \Gamma_{IF} = \Gamma$ and $\Gamma_D \cap \Gamma_N \cap \Gamma_{IF} = \emptyset$. As usual, the Dirichlet and Neumann boundary conditions are

$$\mathbf{v} - \bar{\mathbf{v}} = \mathbf{0} \quad \text{on } \Gamma_D \times (0,T] \ , \tag{4a}$$

$$\boldsymbol{\sigma} \cdot \mathbf{n} - \bar{\mathbf{t}} = \mathbf{0} \quad \text{on } \Gamma_N \times (0,T] \ , \tag{4b}$$

being $\bar{\mathbf{v}}$ the prescribed wall velocity, $\bar{\mathbf{t}}$ the traction to be imposed and $\mathbf{n}$ the outward unit normal vector. For the sake of generality, on Γ_{IF} we opt for a Navier-slip boundary condition, which is nothing but a simple wall model that behaves linearly according to the slip length parameter ε. In this regard, we note that the standard pure stick (*i.e.*, no-slip) condition is recovered as $\varepsilon \to 0$. Similarly, the pure slip condition is recovered as $\varepsilon \to \infty$. It is also interesting to mention that the Navier-slip imposition turns into a standard Dirichlet constraint in the wall normal direction and a Robin-type boundary condition in the tangential one. Hence, we can split the condition to be applied on Γ_{IF} into a normal and tangential contribution as

$$\mathbf{P}^n (\mathbf{v} - \bar{\mathbf{v}}) = \mathbf{0} \quad \text{on } \Gamma_{IF} \times (0,T] \ , \tag{5a}$$

$$\mathbf{P}^t \left(\varepsilon \left(\mathbb{C} \nabla^s \mathbf{v} \right) \cdot \mathbf{n} + \mu \left(\mathbf{v} - \bar{\mathbf{v}} \right) \right) = \mathbf{0} \quad \text{on } \Gamma_{IF} \times (0,T] \ . \tag{5b}$$

μ denotes the effective dynamic viscosity while $\mathbf{P}^n$ and $\mathbf{P}^t$ are the normal and tangential projection operators obtained as

$$\mathbf{P}^n = \mathbf{n} \otimes \mathbf{n}$$

and

$$\mathbf{P}^t = \mathbf{I} - \mathbf{P}^n = \mathbf{I} - \mathbf{p} \otimes \mathbf{n} \ .$$

4.2. Variational form

Prior to the discussion of the variational form, let us first define the notation

$$(a,b)_\Omega = \int_\Omega ab \quad \text{and} \quad (\mathbf{a},\mathbf{b})_\Omega = \int_\Omega \mathbf{ab}$$

for the scalar and vector $L^2(\Omega)$-inner products on the interior of Ω and

$$\langle a,b \rangle_\Gamma = \int_\Gamma ab \quad \text{and} \quad \langle \mathbf{a},\mathbf{b} \rangle_\Gamma = \int_\Gamma \mathbf{ab}$$

for the boundary ones on Γ. Complementary, we also introduce the functional spaces $\boldsymbol{V} := \boldsymbol{H}^1_0(\Omega)$ (*i.e.*, the space of functions in $\boldsymbol{H}^1(\Omega)$ vanishing on Γ_D) and $Q := L^2(\Omega)/\mathbb{R}$ (*i.e.*, the space of square-integrable functions in $\mathbb{R}$) for the velocity and pressure approximations.

The previously defined functional spaces allow us to define the variational form as follows. Find $\mathbf{u} \in \boldsymbol{V}$ and $p \in Q$ such that

$$\begin{aligned} &\left(\mathbf{w}, \rho \frac{\partial \mathbf{v}}{\partial t} \right)_\Omega + (\mathbf{w}, \rho \mathbf{v} \cdot \nabla \mathbf{v})_\Omega + (\nabla \mathbf{w}, \mathbb{C} \nabla^s \mathbf{v})_\Omega - (\nabla \cdot \mathbf{w}, p)_\Omega - (\mathbf{w}, \rho \mathbf{g})_\Omega \\ &\quad + (q, \nabla \cdot \mathbf{v})_\Omega - \langle \mathbf{w}, \bar{\mathbf{t}} \rangle_{\Gamma_N} \\ &\quad - \langle \mathbf{w}, (\mathbb{C} \nabla^s \mathbf{v} - p\mathbf{I}) \cdot \mathbf{n} \rangle_{\Gamma_{IF}} + \frac{\mu + \beta}{\gamma h} \langle \mathbf{w}, \mathbf{P}^n (\mathbf{v} - \bar{\mathbf{v}}) \rangle_{\Gamma_{IF}} \\ &\quad + \langle \mathbb{C} \nabla^s \mathbf{w} - q\mathbf{I}, \mathbf{P}^n (\mathbf{v} - \bar{\mathbf{v}}) \rangle_{\Gamma_{IF}} \\ &\quad + \frac{1}{\varepsilon + \gamma h} \langle \mathbf{w}, \mathbf{P}^t \left(\varepsilon \left(\mathbb{C} \nabla^s \mathbf{v} \right) \cdot \mathbf{n} + \mu \left(\mathbf{v} - \bar{\mathbf{v}} \right) \right) \rangle_{\Gamma_{IF}} \\ &\quad + \frac{\gamma h}{\varepsilon + \gamma h} \langle (\nabla^s \mathbf{w}) \cdot \mathbf{n}, \mathbf{P}^t \left(\varepsilon \left(\mathbb{C} \nabla^s \mathbf{v} \right) \cdot \mathbf{n} + \mu \left(\mathbf{v} - \bar{\mathbf{v}} \right) \right) \rangle_{\Gamma_{IF}} = 0 \end{aligned} \tag{6}$$

for all $\mathbf{w} \in \boldsymbol{V}$ and $q \in Q$. We shall remark that the variational form in previous equation already includes the Γ_{IF} contributions, which are the usual boundary term coming from the integration by parts of the stress plus the weak imposition of the Navier-slip condition. About the latter, γ is a user-definable penalty constant and β is a stability constant, which value can be found in [64].

For further details on the convergence and stability properties of the Navier-slip Nitsche's technique in Eq. (6) we refer the reader to [64]. Complementary, the extension of such technique to the thin-walled bodies case can be found in [4].

4.3. Discretization and stabilisation

The discrete version of the problem in Eq. (6) is obtained from the partition of Ω into a collection of non-overlapping elements. We shall mention that we only consider simplicial elements, that is to say linear tetrahedra. Furthermore, we also note that a linear interpolation is used for both velocity and pressure fields. This interpolation pair is known to be LBB-unstable and thus requires a stabilisation technique. Among the several alternatives present in the literature, in this work we opt for the Variational MultiScales (VMS) method [65–67], in particular, we use the quasi-static Algebraic SubGrid Scales (ASGS) approach. Considering that the stabilisation is out of the scope of this work as well as the fact that any other option would be equivalently valid, we decided to omit the corresponding terms from the discussion at hand. Nevertheless, we refer the reader to [4] in case these are required.

5. Numerical simulations

This section presents the numerical experiments that we conduct in order to validate the aforementioned methodology. These reproduce four AD scenarios, namely case 1, 2, 3, and 4, coming from real patient-specific medical images. In the following subsections we describe the models setup (geometries, material properties and boundary conditions) and present the obtained results.

5.1. Geometries

In this work we consider four real AD scenarios involving patient-specific medical images. Table 1 presents the AD meshes obtained by applying the segmentation procedure detailed in Section 3.1 to the aforementioned medical images. For the four AD cases we show a render of the volume (*i.e.*, background) mesh in the first table's row, a render of the IF (*i.e.*, surface) mesh in the second one and the result of embedding the IF meshes into the volume ones, that is to say, the discontinuous level set intersections in the third row.

It can be observed that the four ADs present complex geometrical patterns. On the one hand, cases 1 and 2 feature particularly complex IF configurations, either because of the tear(s) positioning (case 1) or its shape and sizing (case 2). Besides this, case 1 becomes particularly challenging as the dissection is developing further towards the brachiocephalic trunk and the left common carotid and subclavian arteries. On the other hand, cases 3 and 4 present a highly dilated FL. To what concerns the presence of reentry tears, these appear in both cases 2 and 4. Despite the presence of such complexities, the proposed methodology manages to effectively represent all the AD scenarios (Table 1).

Besides, it is also interesting to comment on the imperfections appearing at the IF discretization boundary edges. These come from the segmentation of the IF midplane, which reaches the aortic wall as described in Section 3.1. Nevertheless, such imperfections have no affectation to the final calculations as they are automatically filtered by the level set calculation algorithm. Again, this is evinced by the cyan surfaces in Table 1, which depict the zero isosurface of the level set function that is used for the problem resolution.

Complementary, we also collect the mesh features of each one of the cases in Table 2. In this regard, we note that the magnitude that actually matters for the problem resolution is the number of elements of the background mesh. In other words, the skin (*i.e.*, IF) mesh is only used for the calculation of the level set, meaning that it has a purely auxiliary purpose. Finally, we also note that the computational overhead coming from the calculation of the level set is absolutely negligible when compared to the simulation time.

5.2. Material properties

In all the numerical experiments we consider a Newtonian fluid which properties are density $\rho = 1.05 \cdot 10^{-6}$ g/mm^3 and dynamic viscosity $\mu = 3.5 \cdot 10^{-6}$ g/mm s. Hence, the $\mathbb{C}$ tensor in Eq. (2) can be expressed in Voigt notation as

$$\mathbb{C} = \begin{bmatrix} \frac{4\mu}{3} & -\frac{2\mu}{3} & -\frac{2\mu}{3} & 0 & 0 & 0 \\ -\frac{2\mu}{3} & \frac{4\mu}{3} & -\frac{2\mu}{3} & 0 & 0 & 0 \\ -\frac{2\mu}{3} & -\frac{2\mu}{3} & \frac{4\mu}{3} & 0 & 0 & 0 \\ 0 & 0 & 0 & \mu & 0 & 0 \\ 0 & 0 & 0 & 0 & \mu & 0 \\ 0 & 0 & 0 & 0 & 0 & \mu \end{bmatrix}.$$

5.3. Boundary conditions

The boundary conditions are an imposed inflow velocity in the aortic inlet, an imposed outflow velocity in the brachiocephalic trunk as well as in the left subclavian and carotid arteries, a traction free condition in the outlet, and a standard no-slip (*i.e.*, stick) wall condition in both the aortic wall and the IF.

Owing to the lack of further information, we consider the same flow rate profiles in the four AD scenarios (Fig. 4). It must be mentioned that such profiles do not correspond to any of the patients' real ones. Nevertheless, we note that in case of these being available, they could be equivalently applied. Hence, an inflow parabolic velocity distribution is created for each AD scenario from the corresponding ascending aorta flow rate profile in Fig. 4. Similarly, we do so for the outflow velocity profiles of the brachiocephalic trunk and the left carotid and subclavian arteries. The velocity profiles are applied with a time increment of 0.05 s to solve the problem for five complete cycles of 0.87 s, resulting in a total simulation time of 4.35 s.

5.4. Results

The results described in this section have been obtained with the KratosMultiphysics open-source finite element framework (Kratos) [68,69]. Among other capabilities, Kratos implements the level set and CutFEM techniques required in this work as well as the nonlinear (Newton–Raphson) solution strategy, which leverages the highly efficient AMGCL [70,71] algebraic multigrid iterative linear solver. All the simulations have been run in a desktop machine equipped with a 12th Generation Intel® Core™ i9-12900 processor. Both preprocessing and and mesh generation have been done by means of the GiDsimulation software (GiD) [72,73]. GiD has been also used for the postprocessing together with ParaView [74]. For each AD case, we present three horizontal cross-sections (proximal, mid and distal) as well as a frontal one at three time instants representative of the cardiac cycle. Specifically, we discuss the velocity and pressure results obtained at $t = 3.6$ s, $t = 3.9$ s and $t = 4.2$ s, which correspond to the systolic phase, the dicrotic notch and the diastolic phase of the fifth (last) cardiac cycle. Furthermore, we also present a snapshot of the streamlines at $t = 3.6$ s and $t = 4.2$ s for each one of the AD scenarios.

Considering that the pressure jump between the TL and the FL is an extremely valuable indicator of the AD status as well as of its potential evolution, we start the results discussion by analysing the obtained pressure fields. First, we observe large pressure fluctuations in scenarios 1 and 3, which feature a main solitary tear (Figs. 6 and 10). On the contrary, in cases 2 and 4 (Figs. 8 and 12) the large reentry tears result in a more homogeneous pressure distribution across both lumina (TL and FL). It is also interesting to comment on the differences between cases 2 and 4 since these both feature distal tear(s) but with a quite different proximal tear. While in case 2 the proximal (entry) tear is large, which results in a much homogeneous velocity distribution (Fig. 7), in case 4 the entry tear is much smaller, leading to a jet-like velocity and pressure distributions (Figs. 11 and 12). As it is discussed in [75], the abrupt pressure variations between the TL and the FL combined with the location of small tears in the aortic arch are signals of potential aortic enlargement. This phenomenon, but without the reentry tear, can be also observed in case 3, in which the FL enlargement is even more evident (Figs. 9 and 10). Furthermore, we dare say that case 1 is pretty similar to 3 in this regard, but still at a preliminary stage. As discussed in [76], elevated pressure within the FL (Fig. 6) may turn into AD enlargement, and thus constriction of the TL, with potential risk of rupture.

To what concerns the velocity fields, we note that the proposed methodology is able to accurately capture the flow patterns arising from the AD. We consider this a direct consequence of our two-step segmentation proposal, which makes possible to precisely determine the complicated three-dimensional shapes appearing in real (patient-specific) tears. Such proper representation of the IF geometry allows the study of the correlation between the tears' geometrical features and the inflow from the TL to the FL, which directly influences the evolution of the AD. Hence, we observe that in cases 1 (Fig. 5) and 3 (Fig. 9), which feature a relatively small tear, the TL to FL inflow occurs at a high velocity that may cause an elongation of the FL. As commented in previous paragraph, such elongation produces an imbalance between the velocity and pressure waves, which at the same time can affect the blood flow dynamics and contribute to the growth of the FL, something that can eventually affect the haemodynamics of the suprarenal and iliac arteries. Focusing on case 4, we observe that the enlargement of the FL led to the formation of a new reentry tear near to the external aortic wall. This results in a modification in the flow dynamics that turns into a less pronounced midplane enlargement than that of case

Table 1
Preprocess snapshots of the different AD scenarios. First row: render view of the mesh resulting from the outer wall segmentation (first step, see Section 3.1). Second row: render view of the mesh resulting from the IF segmentation (second step, see Section 3.1). Third row: distance function isosurface (cyan) representing the IF.

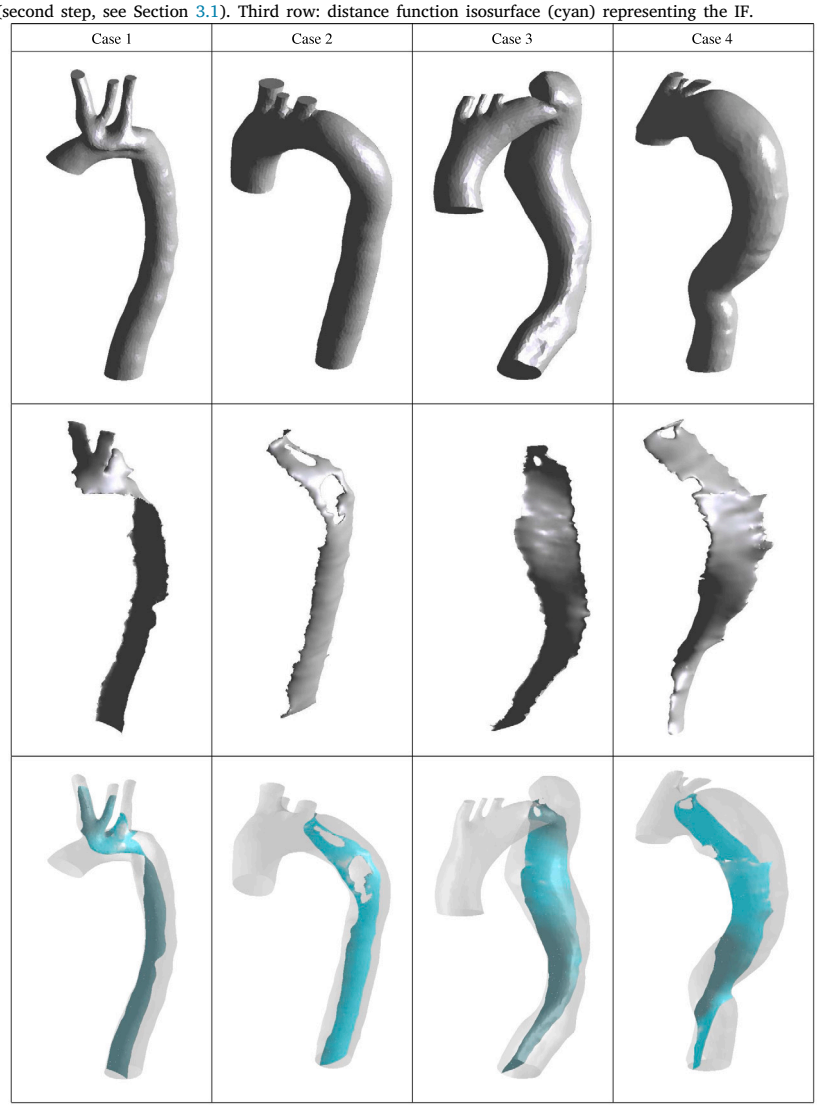

Table 2
Number of elements of IF (triangles) and background (tetrahedra) meshes and simulation elapsed times.

	Case 1	Case 2	Case 3	Case 4
IF mesh	5.1 K	6.3 K	11.9 K	36.8 K
Background mesh	2.3 M	2.3 M	3 M	3 M
Simulation elapsed time	46 min 16 s	26 min 20 s	32 min 48 s	31 min 7 s

2. Nevertheless, the recirculation occurring between the proximal and distal tears might have influenced the growth in the proximal region. This same phenomenon can be noticed in case 2 as well, but with a less pronounced effect owing to the proximity of the entry and reentry tears. To what concerns the affectation of the AD evolution to the flow, the streamlines (Fig. 13) reveal that in less developed ADs (cases 1 and 2) the FL flow is more streamlined. Contrariwise, those patients with highly developed ADs (cases 3 and 4) present more vortical flow structures in the FL.

Last but important, we would like to spend some words regarding the calculation elapsed times, which are collected in Table 2. As it can be observed, the times range from 26 min (case 2) to 46 min (case 1). It is important to note that the computation times are comparable to those of traditional CFD simulations, demonstration the satisfactory performance of our implementation.

6. Discussion

It is widely known that one of the main challenges appearing in the numerical simulation of patient-specific ADs is the generation of the computational model. Typically, this involves generating a separate segmentation of the TL and FL, which must then be combined to obtain the final AD configuration. This combination requires to expand the previously obtained TL model by following a series of boolean operations, which must ensure that the resulting IF features a uniform thickness [26,77–79]. Besides requiring the use of different image/CAD

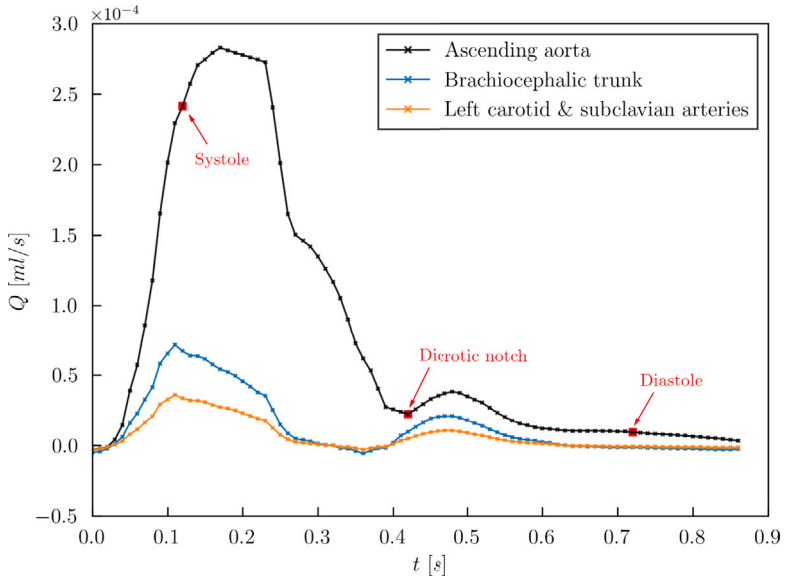

Fig. 4. Flow rate profiles. The solid lines represent the ascending aorta inflow flow rate profile as well as the brachiocephalic trunk and left carotid and subclavian arteries outlet flow rates for one cardiac cycle. The red square markers highlight the time location of the snapshots used for the results assessment.

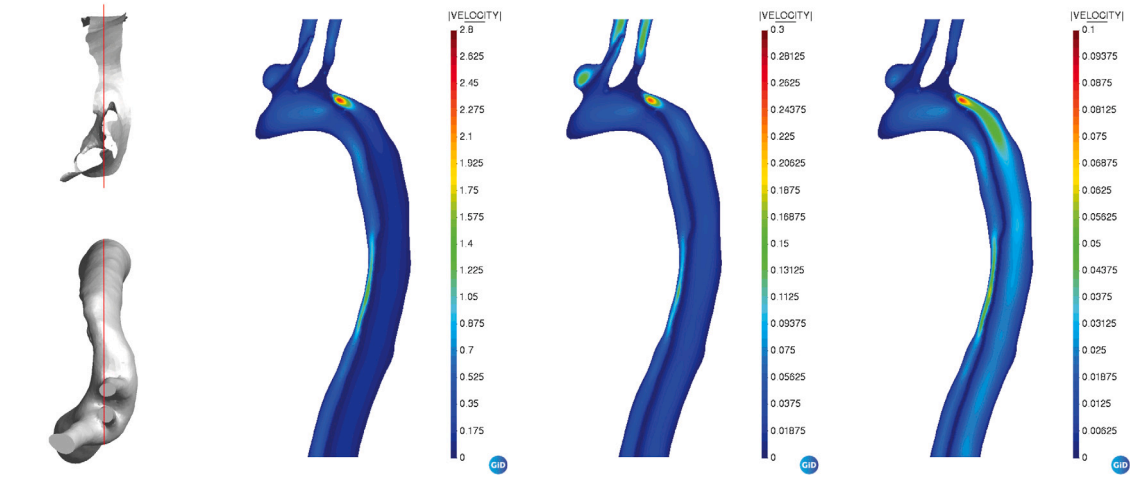

(a) Cross-section location. (b) t = 3.6 s (systole). (c) t = 3.9 s (dicrotic notch). (d) t = 4.2 s (diastole).

Fig. 5. Case 1 velocity modulus (mm^3/s) frontal cross-section at three different instants of a cardiac cycle.

processing programs, such operations often become very complex and time consuming.

The two-step procedure we are proposing greatly simplifies the preprocess by completely avoiding such operations. Instead, we only require two segmentation: the entire aorta (TL and FL) and the IF midline. Though including the extra IF segmentation might seem a great disadvantage, we shall remark that it is straightforward and did not take more than a few minutes for any of the cases in this work. Furthermore, we believe that integrating image processing machine learning techniques [80] has the potential to improve the segmentation accuracy and enhance the scalability of the method for broader clinical applications. Additionally, we also note that our approach avoids any manual operation after the medical images have been segmented, as the distance representation of the IF is automatically handled by the level set algorithm. Furthermore, we bypass all the common errors associated to the volume mesh generation around thin-walled structures. Altogether, our approach results in a much more efficient simulation pipeline that reduces the AD modelling times.

It is also important to note that our methodology has no restrictions on the size of the elements, meaning that it allows the for the mesh refinement in specific areas of interest such as tears or the arterial wall. In addition, our method also facilitates the simulation of various scenarios without modifying (*i.e.*, remeshing) the possibly large background mesh by simply updating the IF surface one, which is much easier to handle and generate. We think that this will allow clinicians to more accurately predict the outcomes of different surgical approaches, such as aortic fenestration or tear occlusion, and potentially reduce the risks associated to them. The capability to easily update the surface mesh, whether for fenestration or patching of tears, allows for to quickly establishing modified IF models. For the sake of clarity, let us for instance consider the case of the aortic fenestration. Aortic fenestration, which is designed to alleviate high pressures in hypertensive FLs and thus the risk of dilation, consists in creating an incision in the IF to redirect blood flow from the FL to the TL. Hence, our approach allows for easy creation and simulation of virtual fenestrations by simply removing the surface elements close to a certain location of the IF. Indeed, this can be automatically done from the radius and the approximate location of the fenestration as it is discussed in [27].

In terms of reliability, we observe that our method's results are consistent with those reported in previous patient-specific computational

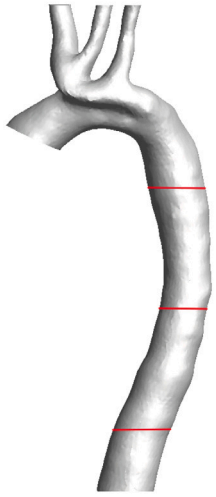

(a) Cross-sections location.

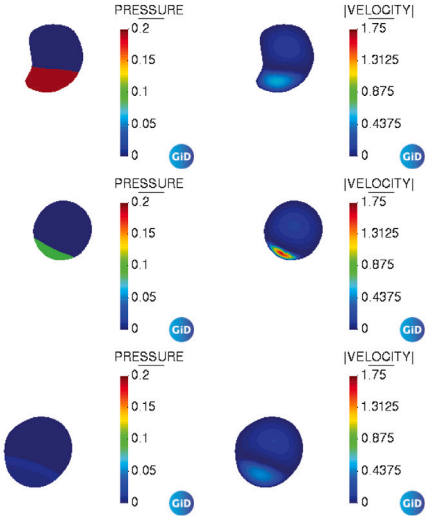

(b) t = 3.6 s (systole).

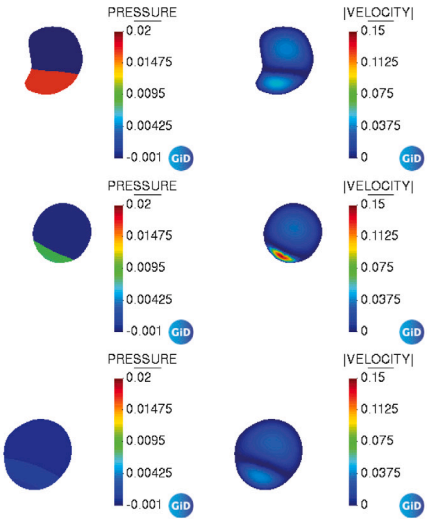

(c) t = 3.9 s (dicrotic notch).

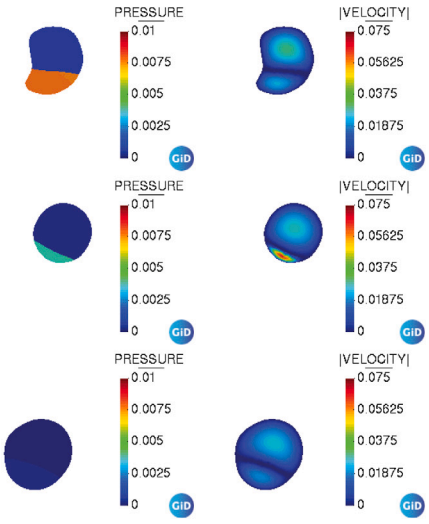

(d) t = 4.2 s (diastole).

Fig. 6. Case 1 pressure (Pa) and velocity modulus (mm^3/s) horizontal cross-sections at three different instants of a cardiac cycle. From top to bottom, the cross-sections are sorted as proximal, mid and distal.

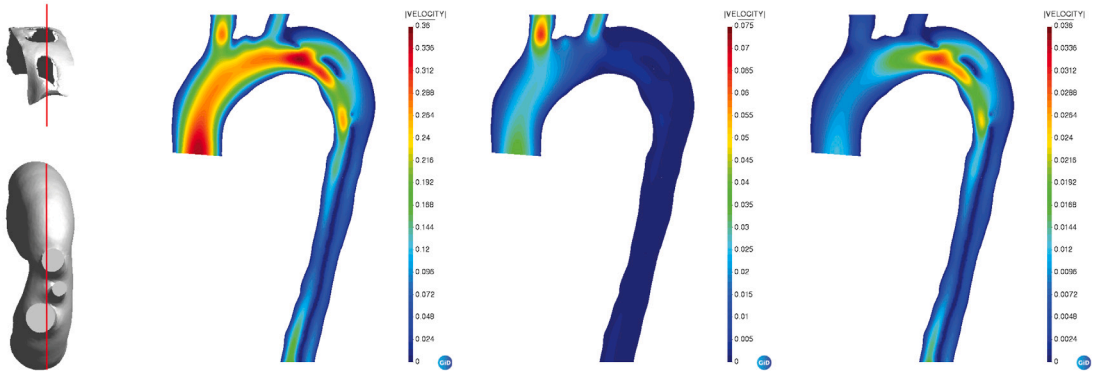

(a) Cross-section location. (b) t = 3.6 s (systole). (c) t = 3.9 s (dicrotic notch). (d) t = 4.2 s (diastole).

Fig. 7. Case 2 velocity modulus (mm^3/s) frontal cross-section at three different instants of a cardiac cycle.

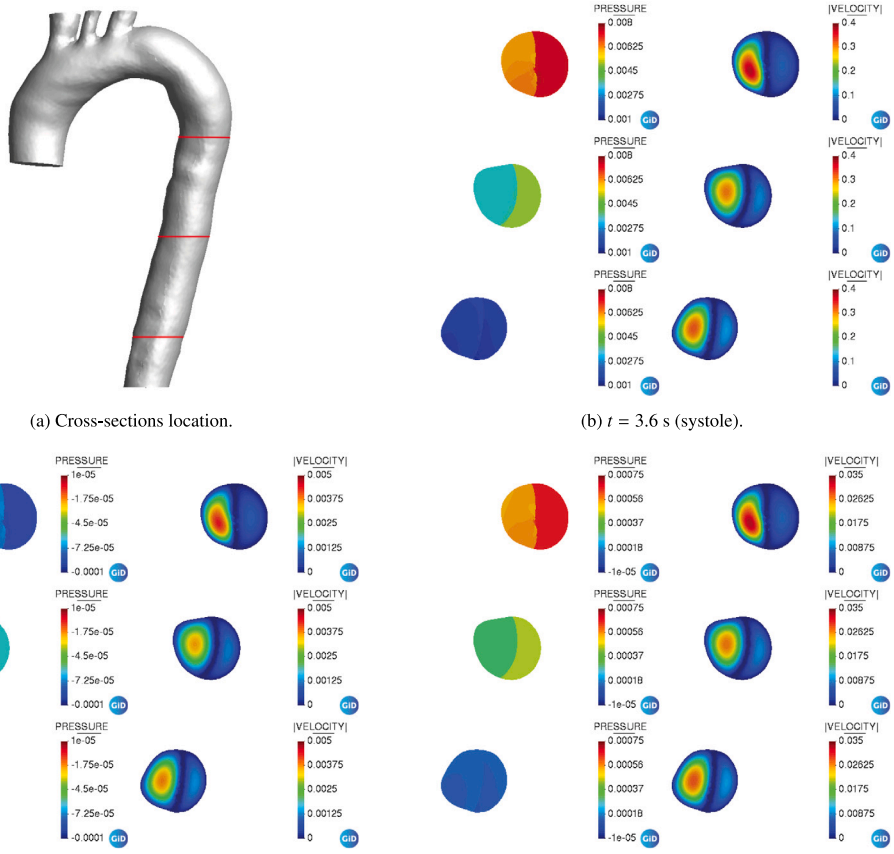

(a) Cross-sections location. (b) t = 3.6 s (systole).

(c) t = 3.9 s (dicrotic notch). (d) t = 4.2 s (diastole).

Fig. 8. Case 2 pressure (Pa) and velocity modulus (mm^3/s) horizontal cross-sections at three different instants of a cardiac cycle. From top to bottom, the cross-sections are sorted as proximal, mid and distal.

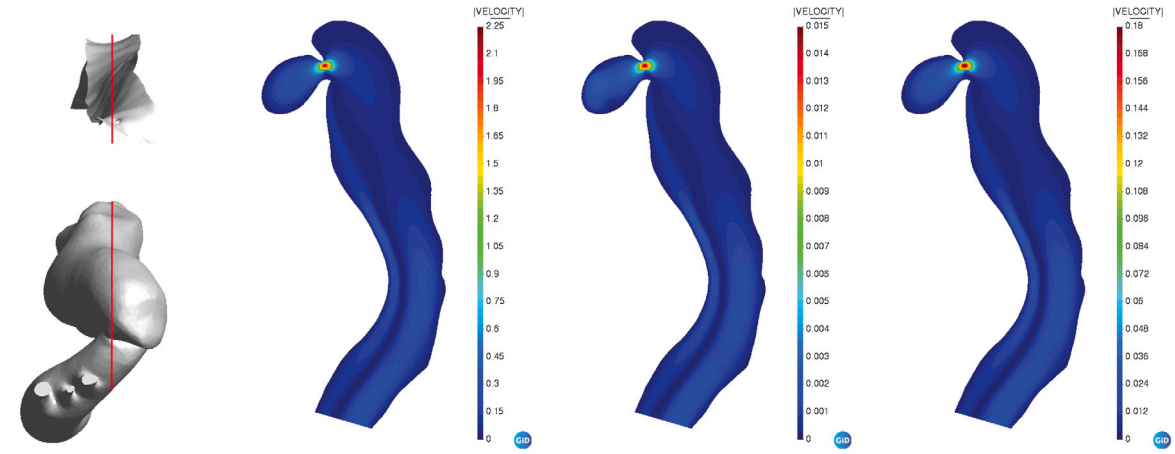

(a) Cross-section location. (b) t = 3.6 s (systole). (c) t = 3.9 s (dicrotic notch). (d) t = 4.2 s (diastole).

Fig. 9. Case 3 velocity modulus (mm^3/s) frontal cross-section at three different instants of a cardiac cycle.

studies [75,76,81,82]. Besides, they align also with the conclusions found in studies such as [83,84], where the authors employed the 4D-Flow MRI technique to predict aortic dilatation and rupture in AD. Hence, we observe that less developed ADs present more laminar flow patterns in the FL, something that indicates a more stable condition of the AD. Contrariwise, patients with more developed ADs feature higher vorticity flows, with the subsequent higher risk of complications. Therefore, we can conclude that using our two-step segmentation plus CutFEM approach has no practical implication from the perspective of velocity and pressure fields.

At this point, it is important to discuss the rigid IF assumption, which is of course a limitation of our approach that overlooks the IF potential deformations as well as their impact on the haemodynamic predictions. In this regard, we should bear in mind that the increased numerical effort required for the FSI modelling is reported to be five to twenty times greater than that of rigid wall simulations [77].

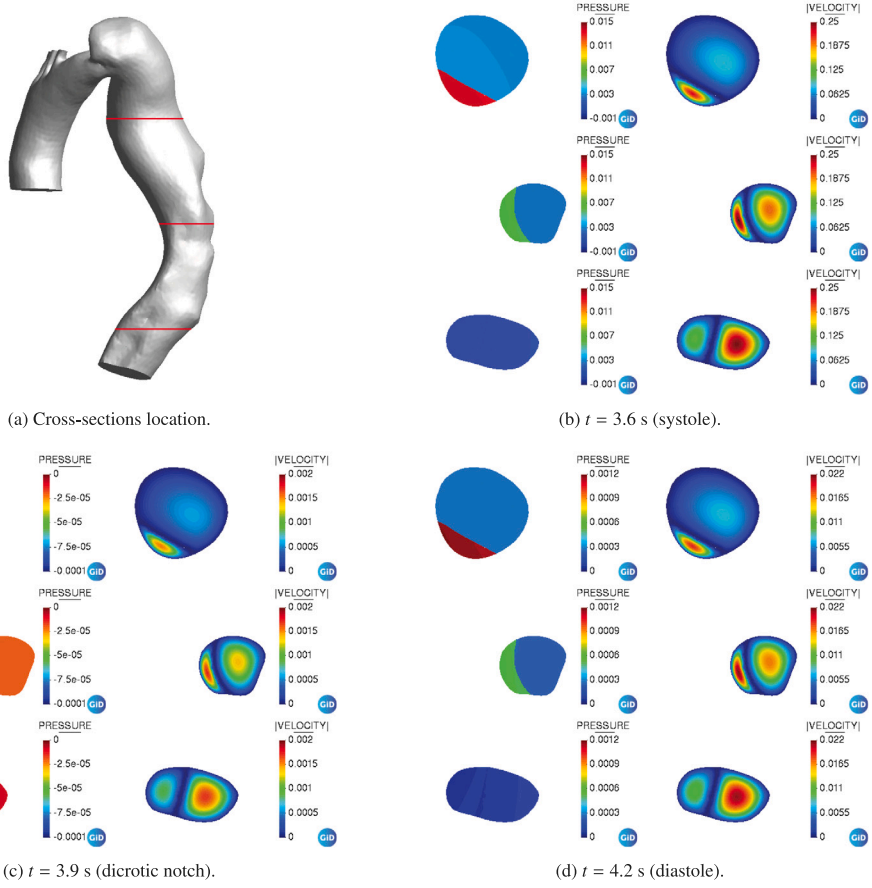

(a) Cross-sections location. (b) t = 3.6 s (systole).

(c) t = 3.9 s (dicrotic notch). (d) t = 4.2 s (diastole).

Fig. 10. Case 3 pressure (Pa) and velocity modulus (mm^3/s) horizontal cross-sections at three different instants of a cardiac cycle. From top to bottom, the cross-sections are sorted as proximal, mid and distal.

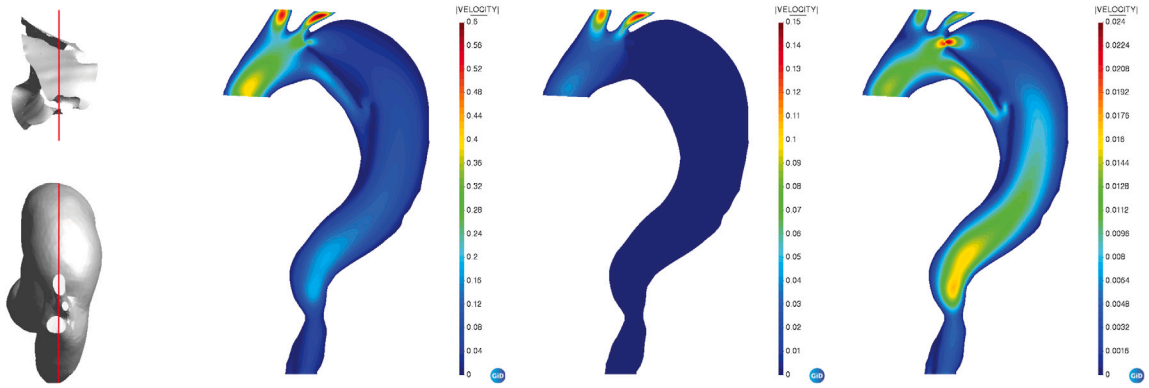

(a) Cross-section location. (b) t = 3.6 s (systole). (c) t = 3.9 s (dicrotic notch). (d) t = 4.2 s (diastole).

Fig. 11. Case 4 velocity modulus (mm^3/s) frontal cross-section at three different instants of a cardiac cycle.

Similarly, [26] reports an increment in the simulation times between eight to ten times. Recent findings indicate that certain haemodynamic indicators (*e.g.*, shear stress-based biomarkers) can be properly modelled using rigid wall simulations [77]. This is the same for predicting the aortic dilation in surgically repaired ADs, obtaining the pressure difference between TL and FL with a rigid wall CFD approach is likely sufficient. Furthermore, it might not be feasible to conduct FSI simulations in a large cohort study. However, it is undoubtedly true that including the movement of the aortic vessel and IF leads to a more accurate estimation of the TL and FL pressure drop, besides providing a better comprehension on the AD initiation, propagation and rupture underlying mechanisms [22–26].

We want to emphasize that our method has no technical limitation in this regard, meaning that our proposal can be perfectly extended to account for the deformation of the IF, making the FSI analysis the most immediate further research line. For that purpose, we conceive two different approaches. The first, and more traditional one, is to follow the approach in [6] in order to apply current methodology in the resolution of a fully coupled FSI problem in which the CFD and the structural (the IF) domains are solved together. This would require knowing the mechanical properties of the IF, which are challenging to estimate [77]. This difficulty leads us to the second approach, that is to directly impose the movement of the IF, obtainable by 4D-PC-MRI [82, 85–87]. This simplifies the FSI problem to a moving boundaries CFD

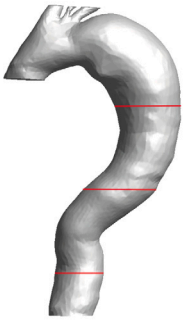

(a) Cross-sections location.

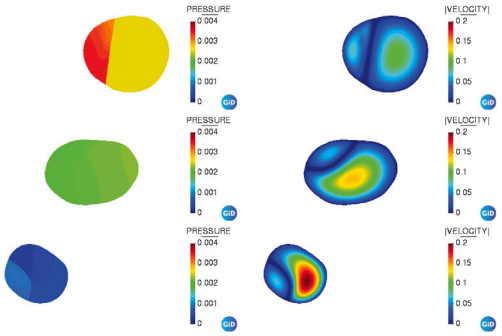

(b) t = 3.6 s (systole).

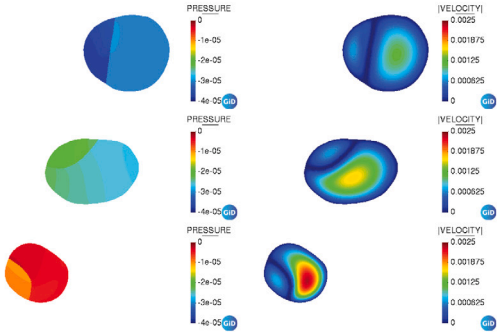

(c) t = 3.9 s (dicrotic notch).

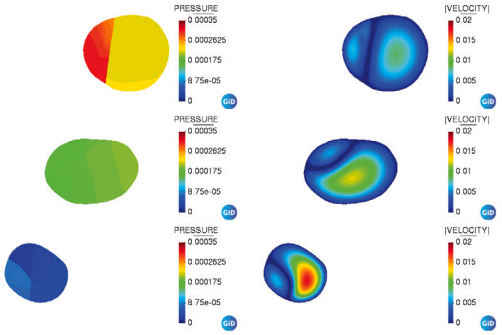

(d) t = 4.2 s (diastole).

Fig. 12. Case 4 pressure (Pa) and velocity modulus (mm^3/s) horizontal cross-sections at three different instants of a cardiac cycle. From top to bottom, the cross-sections are sorted as proximal, mid and distal.

one that does not require solving the IF mechanical problem. On top of resulting in a much simpler simulation, this completely circumvents the need to obtain the IF mechanical properties. Finally, we also note that the moving boundaries CFD approach also opens the possibility of virtually estimating the patient-specific IF material parameters by solving an inverse problem from the imposed IF movement and the obtained pressure field.

7. Conclusion

The objective of this work is to develop a robust and efficient methodology for the accurate CFD analysis of patient-specific ADs. To achieve this, we conceive a novel two-step segmentation process that significantly improves the simulation pipeline without compromising the precision of the AD numerical simulation. Specifically, we use a discontinuous level set technique to introduce a representation of the IF that, in combination with a suitable CutFEM approach, makes it possible to represent the velocity and pressure discontinuities appearing at the IF, as well as to impose the IF wall conditions. The obtained results showcase the capabilities of the proposed CutFEM technique to handle complex patient-specific AD geometries. Furthermore, although this is not a clinical study, the outcomes from using our methodology in four patient-specific cases are consistent with those in similar computational and experimental studies [75,76,81–84]. Such agreement is remarkably achieved without the complexity typically associated with AD model generation, highlighting the robustness and efficiency of our proposal. The presented methodology represents a significant step forward in the simulation of patient-specific ADs, offering accuracy, efficiency and less time consuming model generation. This study also sets a foundation for further innovations in the modelling of complex CVDs using unfitted approaches.

CRediT authorship contribution statement

Rubén Zorrilla: Writing – review & editing, Writing – original draft, Visualization, Validation, Supervision, Software, Methodology.

Eduardo Soudah: Writing – review & editing, Writing – original draft, Validation, Methodology, Funding acquisition, Conceptualization.

Declaration of competing interest

The authors declare that they have no known competing financial interests or personal relationships that could have appeared to influence the work reported in this paper.

Data availability

Data will be made available on request.

Declaration of Generative AI and AI-assisted technologies in the writing process

The authors declare that neither generative AI nor AI-assisted technologies have been used in this work.

Acknowledgements

The authors acknowledge financial support from the Spanish Ministry of Economy and Competitiveness, through the “Severo Ochoa Programme for Centres of Excellence in R&D” (CEX2018-000797-S). Eduardo Soudah acknowledges the support of “Proyecto CPP2021-008546 financiado por MCIN/AEI/10.13039/501100011033 *y* por la Unión Europea NextGenerationEU/ PRTR” and “Proyecto PID2021-122518OB-I00 financiado por MCIN/AEI/ 10.13039/501100011033 *y* por FEDER Una manera de hacer Europa”. Finally, the authors gratefully thank Aortyx and Mr. Yago Trias for the collaboration in the segmentation of the four patient-specific scenarios.

(a) Case 1.

(b) Case 2.

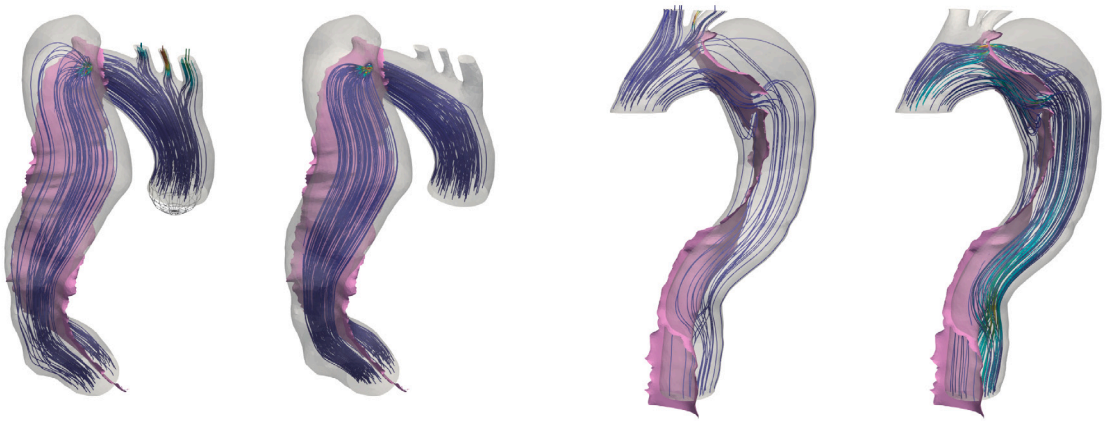

(c) Case 3.

(d) Case 4.

Fig. 13. Streamlines of the four different AD scenarios. For each case, the left and right figures show the streamlines at $t = 03.6$ s (systole) and $t = 4.2$ s (diastole). The streamlines are superimposed on both AD volume (grey) and IF surface (magenta) meshes, also shown first and second rows in Table 1.

References

[1] V. Aboyans, M. Boukhris, Dissecting the epidemiology of aortic dissection, Eur. Heart J. Acute Cardiovasc. Care 10 (7) (2021) 710–711.

[2] I.H. Melvinsdottir, S.H. Lund, B.A. Agnarsson, K. Sigvaldason, T. Gudbjartsson, A. Geirsson, The incidence and mortality of acute thoracic aortic dissection: results from a whole nation study, Eur. J. Cardio-Thorac. Surg. 50 (6) (2016) 1111–1117.

[3] R. Zorrilla, A. Larese, R. Rossi, A modified finite element formulation for the imposition of the slip boundary condition over embedded volumeless geometries, Comput. Methods Appl. Mech. Engrg. 353 (2019) 123–157.

[4] R. Zorrilla, A. Larese de Tetto, R. Rossi, A discontinuous nitsche-based finite element formulation for the imposition of the Navier-slip condition over embedded volumeless geometries, Internat. J. Numer. Methods Fluids 93 (9) (2021) 2968–3003.

[5] S. Osher, R. Fedkiw, Level Set Methods and Dynamic Implicit Surfaces, Springer.

[6] R. Zorrilla, R. Rossi, R. Wüchner, E. Oñate, An embedded finite element framework for the resolution of strongly coupled fluid–structure interaction problems. Application to volumetric and membrane-like structures, Comput. Methods Appl. Mech. Engrg. 368 (2020) 113179.

[7] K.-X. Qing, Y.C. Chan, S.F. Lau, W.-K. Yiu, A.C.W. Ting, S.W.K. Cheng, Ex-vivo haemodynamic models for the study of stanford type B aortic dissection in isolated porcine aorta, Eur. J. Vasc. Endovascular Surg. 44 (4) (2012) 399–405.

[8] E.M. Faure, L. Canaud, P. Cathala, I. Serres, C. Marty-Ané, P. Alric, Human ex-vivo model of stanford type B aortic dissection, J. Vasc. Surg. 60 (3) (2014) 767–775.

[9] T. Tsai, M. Schlicht, K. Khanafer, J. Bull, D. Valassis, W. D., R. Berguer, E. K., Tear size and location impacts false lumen pressure in an ex vivo model of chronic type B aortic dissection, J. Vasc. Surg. 47 (4) (2008) 844–851.

[10] P. Rudenick, B. Bijnens, D. García-Dorado, A. Evangelista, An in vitro phantom study on the influence of tear size and configuration on the hemodynamics of the lumina in chronic type B aortic dissections, J. Vasc. Surg. 57 (2) (2013) 464–474.

[11] S. Peelukhana, Y. Wang, Z. Berwick, J. Kratzberg, J. Krieger, B. Roeder, R. Cloughs, A. Hsiao, S. Chambers, G. Kassab, Role of pulse pressure and geometry of primary entry tear in acute type B dissection propagation, Ann. Biomed. Eng. 45 (3) (2017) 592–603.

[12] S. Marconi, E. Lanzarone, H. De Beaufort, M. Conti, S. Trimarchi, F. Auricchio, A novel insight into the role of entry tears in type B aortic dissection: pressure measurements in an in vitro model, Int. J. Artif. Organs 40 (10) (2017) 563–574.

[13] E. Soudah, P. Rudenick, M. Bordone, B. Bijnens, D. García-Dorado, A. Evangelista, E. Oñate, Validation of numerical flow simulations against in vitro phantom measurements in different type B aortic dissection scenarios, Comput. Methods Biomech. Biomed. Eng. 18 (8) (2015) 805–815.

[14] S. Ben Ahmed, D. Dillon-Murphy, C. Figueroa, Computational study of anatomical risk factors in idealized models of type B aortic dissection, Eur. J. Vasc. Endovascular Surg. 52 (6) (2016) 736–745.

[15] P.A. Rudenick, M. Bordone, B.H. Bijnens, E. Soudah, E. Oñate, D. Garcia-Dorado, A. Evangelista, A multi-method approach towards understanding the pathophysiology of aortic dissections – The complementary role of in-silico, in-vitro and in-vivo information, in: O. Camara, M. Pop, K. Rhode, M. Sermesant, N. Smith, A. Young (Eds.), Statistical Atlases and Computational Models of the Heart, Springer Berlin Heidelberg, Berlin, Heidelberg, 2010, pp. 114–123.

[16] K.M. Tse, P. Chiu, H.P. Lee, P. Ho, Investigation of hemodynamics in the development of dissecting aneurysm within patient-specific dissecting aneurismal aortas using computational fluid dynamics (CFD) simulations, J. Biomech. 44 (5) (2011) 827–836.

[17] W.N. Wan ab Naim, P.B. Ganesan, Z. Sun, K. Osman, E. Lim, Impact of the number of tears in patient-specific type B aortic dissecting aneurysm: CFD simulation, J. Mech. Med. Biol. 14 (02) (2014) 1450017.
[18] C.H. Armour, B. Guo, S. Saitta, S. Pirola, Y. Liu, Z. Dong, X.Y. Xu, Evaluation and verification of patient-specific modelling of type B aortic dissection, Comput. Biol. Med. 140 (2022) 105053.
[19] H. Chen, S. Peelukhana, Z. Berwick, J. Kratzberg, J. Krieger, B. Roeder, S. Chambers, G. Kassab, Fluid–structure interaction simulations of aortic dissection with bench validation, J. Vasc. Surg. 64 (6) (2016) 1892.
[20] P. Ryzhakov, E. Soudah, N. Dialami, Computational modeling of the fluid flow and the flexible intimal flap in type B aortic dissection via a monolithic arbitrary Lagrangian/Eulerian fluid-structure interaction model, Int. J. Numer. Methods Biomed. Eng. 35 (11) (2019) e3239.
[21] M.Y. Chong, B. Gu, B.T. Chan, Z.C. Ong, X.Y. Xu, E. Lim, Effect of intimal flap motion on flow in acute type B aortic dissection by using fluid-structure interaction, Int. J. Numer. Methods Biomed. Eng. 36 (2020) e3399.
[22] M. Alimohammadi, J.M. Sherwood, M. Karimpour, O. Agu, S. Balabani, V. Díaz-Zuccarini, Aortic dissection simulation models for clinical support: fluid-structure interaction vs. rigid wall models, BioMed. Eng. OnLine 14 (1) (2015) 34.
[23] A. Qiao, W. Yin, B. Chu, Numerical simulation of fluid-structure interaction in bypassed DeBakey III aortic dissection, Comput. Methods Biomech. Biomed. Eng. 18 (2015) 1173–1180.
[24] K. Bäumler, V. Vedula, A.M. Sailer, J. Seo, P. Chiu, G. Mistelbauer, F.P. Chan, M.P. Fischbein, A.L. Marsden, D. Fleischmann, Fluid-structure interaction simulations of patient-specific aortic dissection, Biomech. Model. Mechanobiol. 19 (5) (2020) 1607–1628.
[25] J. Zimmermann, K. Bäumler, M. Loecher, T.E. Cork, F.O. Kolawole, K. Gifford, et al., Quantitative hemodynamics in aortic dissection: Comparing in vitro MRI with FSI simulation in a compliant model, in: International Conference on Functional Imaging and Modeling of the Heart, Springer, 2021, pp. 575–586.
[26] Y. Zhu, S. Mirsadraee, U. Rosendahl, J. Pepper, X.Y. Xu, Fluid-structure interaction simulations of repaired type A aortic dissection: a comprehensive comparison with rigid wall models, Front. Physiol. 13 (2022) 913457.
[27] R. Zorrilla, E. Soudah, R. Rossi, Computational modeling of the fluid flow in type B aortic dissection using a modified FE embedded formulation, Biomech. Model. Mechanobiol. 19 (2020) 1565–1583.
[28] T. Sawada, A. Tezuka, LLM and X-FEM based interface modeling of fluid–thin structure interactions on a non-interface-fitted mesh, Comput. Mech. 48 (3) (2011) 319–332.
[29] L. Foucard, F. Vernerey, An X-FEM-based numerical-asymptotic expansion for simulating a Stokes flow near a sharp corner, Internat. J. Numer. Methods Engrg. 102 (2) (2015) 79–98.
[30] B. Schott, S. Shahmiri, R. Kruse, W. Wall, A stabilized nitsche-type extended embedding mesh approach for 3D low- and high-Reynolds-number flows, Internat. J. Numer. Methods Fluids 82 (6) (2016) 289–315.
[31] F. Alauzet, B. Fabrèges, M.A. Fernández, M. Landajuela, Nitsche-XFEM for the coupling of an incompressible fluid with immersed thin-walled structures, Comput. Methods Appl. Mech. Engrg. 301 (2016) 300–335.
[32] C. Peskin, The immersed boundary method, Acta Numer. 112 (2002) 479–517.
[33] L. Zhang, A. Gerstenberger, X. Wang, W.K. Liu, Immersed finite element method, Comput. Methods Appl. Mech. Engrg. 193 (21) (2004) 2051–2067.
[34] R. Löhner, J.D. Baum, E. Mestreau, D. Sharov, C. Charman, D. Pelessone, Adaptive embedded unstructured grid methods, Internat. J. Numer. Methods Engrg. 60 (3) (2004) 641–660.
[35] R. Löhner, J. Cebral, F. Camelli, S. Appanaboyina, J. Baum, E. Mestreau, O. Soto, Adaptive embedded and immersed unstructured grid techniques, Comput. Methods Appl. Mech. Engrg. 197 (25) (2008) 2173–2197.
[36] R. Mittal, H. Dong, M. Bozkurttas, F. Najjar, A. Vargas, A. von Loebbecke, A versatile sharp interface immersed boundary method for incompressible flows with complex boundaries, J. Comput. Phys. 227 (10) (2008) 4825–4852.
[37] J.H. Seo, R. Mittal, A sharp-interface immersed boundary method with improved mass conservation and reduced spurious pressure oscillations, J. Comput. Phys. 230 (19) (2011) 7347–7363.
[38] E. Burman, S. Claus, P. Hansbo, M.G. Larson, A. Massing, CutFEM: Discretizing geometry and partial differential equations, Internat. J. Numer. Methods Engrg. 104 (7) (2015) 472–501.
[39] A. Main, G. Scovazzi, The shifted boundary method for embedded domain computations. Part I: Poisson and Stokes problems, J. Comput. Phys. 372 (2018) 972–995.
[40] A. Main, G. Scovazzi, The shifted boundary method for embedded domain computations. Part II: Linear advection-diffusion and incompressible Navier-Stokes equations, J. Comput. Phys. 372 (2018) 996–1026.
[41] R. Zorrilla, R. Rossi, G. Scovazzi, C. Canuto, A. Rodríguez-Ferran, A shifted boundary method based on extension operators, Comput. Methods Appl. Mech. Engrg. 421 (2024) 116782.
[42] L. Boilevin-Kayl, M.A. Fernández, J.-F. Gerbeau, Numerical methods for immersed FSI with thin-walled structures, Comput. & Fluids 179 (2019) 744–763.
[43] C.S. Peskin, Flow patterns around heart valves: A numerical method, J. Comput. Phys. 10 (2) (1972) 252–271.
[44] C.S. Peskin, Numerical analysis of blood flow in the heart, J. Comput. Phys. 25 (3) (1977) 220–252.
[45] B.E. Griffith, X. Luo, D.M. McQueen, C.S. Peskin, Simulating the fluid dynamics of natural and prosthetic heart valves using the immersed boundary method, Int. J. Appl. Mech. 01 (01) (2009) 137–177.
[46] B.E. Griffith, Immersed boundary model of aortic heart valve dynamics with physiological driving and loading conditions, Int. J. Numer. Methods Biomed. Eng. 28 (3) (2012) 317–345.
[47] A.M. Bavo, G. Rocatello, F. Iannaccone, J. Degroote, J. Vierendeels, P. Segers, Fluid-structure interaction simulation of prosthetic aortic valves: Comparison between immersed boundary and arbitrary Lagrangian-Eulerian techniques for the mesh representation, PLoS One 11 (4) (2016) 1–17.
[48] D. Kamensky, M.-C. Hsu, D. Schillinger, J.A. Evans, A. Aggarwal, Y. Bazilevs, M.S. Sacks, T.J. Hughes, An immersogeometric variational framework for fluid–structure interaction: Application to bioprosthetic heart valves, Comput. Methods Appl. Mech. Engrg. 284 (2015) 1005–1053.
[49] D. Kamensky, M.-C. Hsu, Y. Yu, J.A. Evans, M.S. Sacks, T.J. Hughes, Immersogeometric cardiovascular fluid–structure interaction analysis with divergence-conforming B-splines, Comput. Methods Appl. Mech. Engrg. 314 (2017) 408–472.
[50] C. Zhu, J.-H. Seo, R. Mittal, Computational modelling and analysis of haemodynamics in a simple model of aortic stenosis, J. Fluid Mech. 851 (2018) 23–49.
[51] I. Fumagalli, M. Fedele, C. Vergara, L. Dede', S. Ippolito, F. Nicolò, C. Antona, R. Scrofani, A. Quarteroni, An image-based computational hemodynamics study of the systolic anterior motion of the mitral valve, Comput. Biol. Med. 123 (2020) 103922.
[52] A. Aghilinejad, H. Wei, G.A. Magee, N.M. Pahlevan, Model-based fluid-structure interaction approach for evaluation of thoracic endovascular aortic repair endograft length in type B aortic dissection, Front. Bioeng. Biotechnol. 10 (2022).
[53] C.A. Morariu, F. Zohourian, D. Dohle, K. Tsagakis, J. Pauli, Unsupervised extraction of the aortic dissection membrane based on a multiscale piecewise ridge model, in: 2016 IEEE 13th International Symposium on Biomedical Imaging, ISBI, IEEE, 2016, pp. 1368–1371.
[54] C.A. Morariu, T. Terheiden, D.S. Dohle, K. Tsagakis, J. Pauli, Increasing the feasibility of minimally invasive procedures in type a aortic dissections: a framework for segmentation and quantification, Int. J. Comput. Assist. Radiol. Surg. 11 (2016) 243–252.
[55] X. Xu, Z. He, K. Niu, Y. Zhang, H. Tang, L. Tan, An automatic detection scheme of acute stanford type a aortic dissection based on DCNNs in CTA images, in: Proceedings of the 2019 4th International Conference on Multimedia Systems and Signal Processing, 2019, pp. 16–20.
[56] D. Chen, X. Zhang, Y. Mei, F. Liao, H. Xu, Z. Li, Q. Xiao, W. Guo, H. Zhang, T. Yan, J. Xiong, Y. Ventikos, Multi-stage learning for segmentation of aortic dissections using a prior aortic anatomy simplification, Med. Image Anal. 69 (2021) 101931.
[57] R. Ausas, F. Sousa, G. Buscaglia, An improved finite element space for discontinuous pressures, Comput. Methods Appl. Mech. Engrg. 199 (2010) 1019–1031.
[58] J. Nitsche, Über ein Variationsprinzip zur Lösung von Dirichlet-Problemen bei Verwendung von Teilräumen, die keinen Randbedingungen unterworfen sind, Abh. Math. Semin. Univ. Hambg. 36 (1) (1971) 9–15.
[59] R. Codina, J. Baiges, Approximate imposition of boundary conditions in immersed boundary methods, Internat. J. Numer. Methods Engrg. 80 (11) (2009) 1379–1405.
[60] J. Baiges, R. Codina, F. Henke, S. Shahmiri, W.A. Wall, A symmetric method for weakly imposing Dirichlet boundary conditions in embedded finite element meshes, Internat. J. Numer. Methods Engrg. 90 (5) (2012) 636–658.
[61] A. Massing, M. Larson, A. Logg, M. Rognes, A stabilized nitsche fictitious domain method for the Stokes problem, J. Sci. Comput. 61 (3) (2014) 604–628.
[62] A. Massing, B. Schott, W. Wall, A stabilized Nitsche cut finite element method for the Oseen problem, Comput. Methods Appl. Mech. Engrg. 328 (2018) 262–300.
[63] J. Urquiza, A. Garon, M.-I. Farinas, Weak imposition of the slip boundary condition on curved boundaries for Stokes flow, J. Comput. Phys. 256 (2014) 748–767.
[64] M. Winter, B. Schott, A. Massing, W. Wall, A nitsche cut finite element method for the Oseen problem with general Navier boundary conditions, Comput. Methods Appl. Mech. Engrg. 330 (2018) 220–252.
[65] T.J. Hughes, G.R. Feijóo, L. Mazzei, J.-B. Quincy, The variational multiscale method—a paradigm for computational mechanics, Comput. Methods Appl. Mech. Engrg. 166 (1) (1998) 3–24.
[66] Y. Bazilevs, V. Calo, J. Cottrell, T. Hughes, A. Reali, G. Scovazzi, Variational multiscale residual-based turbulence modeling for large eddy simulation of incompressible flows, Comput. Methods Appl. Mech. Engrg. 197 (1) (2007) 173–201.
[67] T.J.R. Hughes, G. Scovazzi, L.P. Franca, Multiscale and stabilized methods, in: Encyclopedia of Computational Mechanics Second Edition, John Wiley & Sons, Ltd, 2017, pp. 1–64.
[68] P. Dadvand, R. Rossi, E. Oñate, An object-oriented environment for developing finite element codes for multi-disciplinary applications, Arch. Comput. Methods Eng. 17 (3) (2010) 253–297.

[69] P. Dadvand, R. Rossi, M. Gil, X. Martorell, J. Cotela, E. Juanpere, S. Idelsohn, E. Oñate, Migration of a generic multi-physics framework to HPC environments, Comput. & Fluids 80 (2013) 301–309.
[70] D. Demidov, AMGCL: An efficient, flexible, and extensible algebraic multigrid implementation, Lobachevskii J. Math. 40 (5) (2019) 535–546.
[71] D. Demidov, AMGCL – A C++ library for efficient solution of large sparse linear systems, Softw. Impacts 6 (2020) 100037.
[72] A. Coll, R. Ribó, M. Pasenau, E. Escolano, J. Perez, A. Melendo, A. Monros, J. Gárate, GiD v.14 Reference Manual, 2018.
[73] A. Coll, R. Ribó, M. Pasenau, E. Escolano, J. Perez, A. Melendo, A. Monros, J. Gárate, GiD v.14 Customization Manual, 2018.
[74] J. Ahrens, B. Geveci, C. Law, in: C.D. Hansen, C.R. Johnson (Eds.), Visualization Handbook, Elsevier Inc., Burlington, MA, USA, 2005, pp. 717–731 (Chapter ParaView: An End-User Tool for Large Data Visualization).
[75] J. Tolenaar, J. van Keulen, S. Trimarchi, F. Jonker, J. van Herwaarden, H. Verhagen, F. Moll, M. B., Number of entry tears is associated with aortic growth in type B dissections, Ann. Thorac. Surg. 96 (1) (2013) 39–42.
[76] B.J. Doyle, P.E. Norman, Computational biomechanics in thoracic aortic dissection: Today's approaches and tomorrow's opportunities, Ann. Biomed. Eng. 44 (1) (2016) 71–83.
[77] R. Schussnig, M. Rolf-Pissarczyk, K. Bäumler, T.-P. Fries, G.A. Holzapfel, M. Kronbichler, On the role of tissue mechanics in fluid–structure interaction simulations of patient-specific aortic dissection, Internat. J. Numer. Methods Engrg. e7478.
[78] K. Bäumler, V. Vedula, A.M. Sailer, J.H. Seo, P. Chiu, G. Mistelbauer, F.P. Chan, M.P. Fischbein, A.L. Marsden, D. Fleischmann, Fluid-structure interaction simulations of patient-specific aortic dissection, Biomech. Model. Mechanobiol. 19 (5) (2020) 1607–1628, Epub 2020 Jan 28.
[79] S. Moretti, F. Tauro, M. Orrico, N. Mangialardi, A. Facci, Comparative analysis of patient-specific aortic dissections through computational fluid dynamics suggests increased likelihood of degeneration in partially thrombosed false lumen, Bioengineering (Basel) 10 (3) (2023) 316.
[80] D. Xiang, J. Qi, Y. Wen, H. Zhao, X. Zhang, J. Qin, X. Ma, Y. Ren, H. Hu, W. Liu, F. Yang, H. Zhao, X. Wang, C. Zheng, ADSeg: A flap-attention-based deep learning approach for aortic dissection segmentation, Patterns 4 (5) (2023) 100727.
[81] G. Franzetti, M. Bonfanti, S. Homer-Vanniasinkam, V. Diaz-Zuccarini, S. Balabani, Experimental evaluation of the patient-specific haemodynamics of an aortic dissection model using particle image velocimetry, J. Biomech. 134 (2022) 110963.
[82] Y. Zhu, X. Xu, U. Rosendahl, J. Pepper, S. Mirsadraee, Advanced risk prediction for aortic dissection patients using imaging-based computational flow analysis, Clin. Radiol. 78 (3) (2023) e155–e165.
[83] K. Takahashi, T. Sekine, Y. Miyagi, S. Shirai, T. Otsuka, S. Kumita, et al., Four-dimensional flow analysis reveals mechanism and impact of turbulent flow in the dissected aorta, Eur. J. Cardio-Thorac. Surg. 60 (2021) 1064–1072.
[84] N. Burris, H. Patel, M. Hope, Retrograde flow in the false lumen: marker of a false lumen under stress? J. Thorac. Cardiovasc. Surg. 157 (2019) 488–491.
[85] D. Dillon-Murphy, A. Noorani, D. Nordsletten, C.A. Figueroa, Multi-modality image-based computational analysis of haemodynamics in aortic dissection, Biomech. Model. Mechanobiol. 15 (4) (2015) 857–876.
[86] A.G. Sherrah, F.M. Callaghan, R. Puranik, R.W. Jeremy, P.G. Bannon, M.P. Vallely, S.M. Grieve, Multi-Velocity encoding Four-Dimensional flow magnetic resonance imaging in the assessment of chronic aortic dissection, Aorta (Stamford) 5 (3) (2017) 80–90.
[87] D. Liu, Z. Fan, Y. Li, N. Zhang, Z. Sun, J. An, A.F. Stalder, A. Greiser, J. Liu, Quantitative study of abdominal blood flow patterns in patients with aortic dissection by 4-dimensional flow MRI, Sci. Rep. 8 (1) (2018) 9111.